Available online at www.sciencedirect.com
SCIENCE DIRECT®
Physics of the Earth and Planetary Interiors 150 (2005) 15–27
PHYSICS OF THE EARTH AND PLANETARY INTERIORS
www.elsevier.com/locate/pepi

Finite element resistivity modelling for three-dimensional structures with arbitrary anisotropy

Yuguo Li[a,*], Klaus Spitzer[b]

[a] *Fachrichtung Geophysik, Freie Universität Berlin, Malteserstrasse 74-100, 12249 Berlin, Germany*
[b] *Institut für Geophysik, TU Bergakademie Freiberg, Gustav-Zeuner-Strasse 12, 09596 Freiberg, Germany*

Received 31 January 2003; received in revised form 24 May 2003; accepted 16 August 2004

Abstract

We present a three-dimensional finite element algorithm for direct current resistivity modelling. The standard Fortran code allows for nearly arbitrary conductivity structures including general anisotropy. The problem is formulated in terms of secondary potentials where mixed boundary conditions are incorporated. Also in case of anisotropy, this type of boundary condition is superior to the Dirichlet type. We have verified the finite element method using an anisotropic two-layered earth, whose analytical solutions are available. For this simple model, the algorithm achieves high accuracy. The relative deviation between numerical and analytical solution is less than 1.2%. Due to the lack of further analytical references, the responses of three representative model types serve as a cross-check for plausibility and prove the operativeness of the code.

Keywords: Electrical anisotropy; Three-dimensional dc resistivity modelling; Finite elements; Singularity removal

1. Introduction

It is widely known that the electric conductivity in the Earth's subsurface shows anisotropic effects. Laboratory studies have revealed strong intrinsic electric anisotropies, e.g., among gneisses or other rock types. Furthermore, fracture zones occurring in the subsurface as a response to local or regional stress regimes often show significant orientational preferences giving rise to a more macroscopic electric anisotropy. However, effects produced by anisotropy are hard to detect in the field. Hence, they are often disregarded. Due to the ill-posedness of the three-dimensional inverse geoelectric problem, it is mostly still possible to find isotropic conductivity models that do match the data but imply wrong structural information. It therefore needs two basic prerequisites to interpret anisotropic structures. Firstly, field surveys have to be designed in a way to detect anisotropy and, secondly, numerical codes have to be developed to calculate the anisotropic response.

As for the field survey design to detect anisotropic features, several azimuthal electrode arrays are proposed, such as square arrays (Habberjam, 1979), az-

* Corresponding author. Present address: IGPP, Scripps Institution of Oceanography, La Jolla, California, USA. Tel.: +1 858 5344238; fax: +1 858 5348090.
E-mail addresses: yuguo@ucsd.edu (Y. Li), klaus.spitzer@geophysik.tu-freiberg.de (K. Spitzer)

0031-9201/$ – see front matter © 2004 Published by Elsevier B.V.
doi:10.1016/j.pepi.2004.08.014

imuthal Wenner and Schlumberger arrays (Leonard-Mayer, 1984; Taylor and Fleming, 1988) as well as azimuthal offset Wenner array (Watson and Barker, 1999). Several successful applications of determining fracture strike orientations have been reported in the literature (e.g., Busby, 2000). However, numerical simulations for geoelectrical fields in anisotropic structures have rarely been discussed in the literature, especially for multidimensional anisotropic structures. The electrical potential due to a point source in a homogeneous anisotropic medium can be obtained by transforming Laplace's equation for a homogeneous isotropic medium into Laplace's equation for a homogeneous anisotropic medium by stretching and rotating a coordinate system (Bhattacharya and Patra, 1968; Habberjam, 1979). The effects of anisotropy for a layered structure was studied by Wait (1990), Li and Uren (1997) and Yin and Weidelt (1999). Verner and Pek (1998) presented a two-dimensional finite difference algorithm for numerical modelling of direct currents in anisotropic structures. Bibby (1978) presented a finite element code for axially symmetric bodies, which allows for some simple cases of anisotropy.

In this paper, a three-dimensional finite element (FE) code is introduced that is able to simulate the electric field of pole or bipole sources in arbitrarily anisotropic environments. In Section 2, we describe the numerical realization of the FE algorithm in detail. We then verify the finite element algorithm using an anisotropic two-layered earth. This is the only model to carry out a quantitative check on accuracy. We further calculate the apparent resistivity of three types of anisotropy, i.e., horizontal, vertical and dipping anisotropy, in order to show the plausibility of the calculated responses. With respect to practical application, we consider the so-called P_2 invariant of the apparent resistivity tensor introduced by Bibby (1986).

2. Governing equations and boundary conditions

We consider a model of the earth with conductivity which varies with both the position and direction. A Cartesian coordinates system (x, y, z) is used, the vertical z-axis points downwards. In the anisotropic earth, the current density $\boldsymbol{j}$ and the electric field $\boldsymbol{E}$ are in general no longer parallel, which is expressed by the generalized Ohm's law

$$\boldsymbol{j} = \underline{\underline{\sigma}}\boldsymbol{E} = \underline{\underline{\rho}}^{-1}\boldsymbol{E}, \tag{1}$$

where

$$\underline{\underline{\sigma}} = \underline{\underline{\rho}}^{-1}, \qquad \underline{\underline{\rho}} = \begin{pmatrix} \rho_{xx} & \rho_{xy} & \rho_{xz} \\ \rho_{yx} & \rho_{yy} & \rho_{yz} \\ \rho_{zx} & \rho_{zy} & \rho_{zz} \end{pmatrix}$$

are the conductivity and the resistivity tensor, respectively. In the earth, these tensors are symmetric and positive definite, and, thus, characterized by only six components (i.e., the upper or lower triangular part). The tensor may be rotated into its principal axes. Then, it is described by its three principal values ρ_1, ρ_2 and ρ_3 and the corresponding Euler angles α, β and γ. The transformation is carried out by successively applying three rotation matrices to the tensor corresponding to the Euler angles: first a rotation around the z-axis by α, then around the new x-axis by β, and finally around the new z-axis by γ. In this way, arbitrary anisotropy may be represented for any coordinate system.

The flow of the steady electric current obeys the equation of continuity, with the current source I at a point (x_q, y_q, z_q), then we have

$$\nabla \cdot \boldsymbol{j}(x, y, z) = I\delta(x - x_q)\delta(y - y_q)\delta(z - z_q), \tag{2}$$

where δ is the Dirac delta function.

The stationary electric field $\boldsymbol{E}$ can be represented by the negative gradient of the electric potential v

$$\boldsymbol{E}(x, y, z) = -\nabla v(x, y, z). \tag{3}$$

Substituting Eqs. (1) and (3) into Eq. (2), we have the following relation

$$\nabla \cdot (\underline{\underline{\rho}}^{-1}(x, y, z)\nabla v(x, y, z)) = -I\delta(x - x_q)\delta(y - y_q)\delta(z - z_q), \tag{4}$$

which is the differential equation of the electric potential $v(x, y, z)$ for a three-dimensional conductivity distribution with general anisotropy. This differential equation is similar to that of the isotropic case, however, the scalar resistivity is turned into its tensor equivalent.

Numerical approximations using Eq. (4) typically give poor results in the vicinity of the source location because of steep gradients around the source. In order to remove the effect of the singular potential caused by

the source, the singularity removal procedure (Lowry et al., 1989; Zhao and Yedlin, 1996) is applied. The potential v is then subdivided into a primary potential v_p caused by the current source in a homogeneous anisotropic half-space with the conductivity tensor $\underline{\underline{\rho_p^{-1}}}$ and a secondary potential v_s caused by the inhomogeneity described by the anomalous conductivity tensor $\underline{\underline{\rho_s^{-1}}}(x,y,z) = \underline{\underline{\bar{\rho}^{-1}}}(x,y,z) - \underline{\underline{\rho_p^{-1}}}$, yielding

$$v(x,y,z) = v_\mathrm{p}(x,y,z) + v_\mathrm{s}(x,y,z). \tag{5}$$

The primary potential v_p satisfies the following partial differential equation

$$\nabla\cdot(\underline{\underline{\rho_p^{-1}}}(x,y,z)\nabla v_\mathrm{p}(x,y,z)) = -I\delta(x-x_\mathrm{q})\delta(y-y_\mathrm{q})\delta(z-z_\mathrm{q}). \tag{6}$$

For a homogeneous, three-axis anisotropic half-space and the current source located at the origin of the coordinate system, the solution of (6) reads (Bhattacharya and Patra, 1968; Habberjam, 1979)

$$v_\mathrm{p} = \frac{I}{2\pi}\frac{(\rho_1^\mathrm{p}\rho_2^\mathrm{p}\rho_3^\mathrm{p})^{1/2}}{B_\mathrm{p}^{1/2}}, \tag{7}$$

with

$$B_\mathrm{p} = \rho_1^\mathrm{p}x^2 + \rho_2^\mathrm{p}y^2 + \rho_3^\mathrm{p}z^2.$$

Here, ρ_1^p, ρ_2^p and ρ_3^p are the principal resistivities of the homogeneous anisotropic half-space. Inserting Eqs. (5) and (6) into (4), gives the differential equation for v_s

$$\nabla\cdot(\underline{\underline{\rho^{-1}}}(x,y,z)\nabla v_\mathrm{s}(x,y,z)) + \nabla\cdot(\underline{\underline{\rho_s^{-1}}}(x,y,z)\nabla v_\mathrm{p}(x,y,z)) = 0. \tag{8}$$

Finally, boundary conditions must be applied. Since no current crosses the ground surface denoted by Γ_s, the boundary conditions on Γ_s are given by

$$\frac{\partial v_\mathrm{p}}{\partial n} = 0, \qquad \frac{\partial v_\mathrm{s}}{\partial n} = 0 \quad \text{on } \Gamma_\mathrm{s}, \tag{9}$$

where n is the outward normal direction of the ground surface Γ_s.

On the other domain boundaries denoted by Γ_∞, homogeneous Dirichlet boundary conditions (i.e., the potentials are set to zero) or Neumann boundary conditions can be used, but it is often found that these assumptions cause under- or overshooting, respectively, in the numerical calculated potentials at some distance from the point source (Coggon, 1971). Dey and Morrison (1979) therefore proposed mixed boundary conditions for an isotropic medium, which use the asymptotical behaviour of the potential and its gradient at large distance from the point source. In an anisotropic case, such mixed boundary conditions can also be derived (see Appendix A for details). They read

$$\underline{\underline{\rho^{-1}}}\frac{\partial v_\mathrm{s}}{\partial n} + \underline{\underline{\rho_s^{-1}}}\frac{\partial v_\mathrm{p}}{\partial n} = -\frac{r\,\cos(r,n)}{B}v_\mathrm{s} + r\,\cos(r,n)v_\mathrm{p}\left(\frac{1}{B_\mathrm{p}} - \frac{1}{B}\right) \quad \text{on } \Gamma_\infty, \tag{10}$$

with

$$\begin{aligned} B_\mathrm{p} &= \rho_{xx}^\mathrm{p}(x-x_\mathrm{q})^2 + 2\rho_{xy}^\mathrm{p}(x-x_\mathrm{q})(y-y_\mathrm{q}) \\ &\quad + 2\rho_{xz}^\mathrm{p}(x-x_\mathrm{q})z + \rho_{yy}^\mathrm{p}(y-y_\mathrm{q})^2 \\ &\quad + 2\rho_{yz}^\mathrm{p}(y-y_\mathrm{q})z + \rho_{zz}^\mathrm{p}z^2, \\ B &= \rho_{xx}(x-x_\mathrm{q})^2 + 2\rho_{xy}(x-x_\mathrm{q})(y-y_\mathrm{q}) \\ &\quad + 2\rho_{xz}(x-x_\mathrm{q})z + \rho_{yy}(y-y_\mathrm{q})^2 \\ &\quad + 2\rho_{yz}(y-y_\mathrm{q})z + \rho_{zz}z^2. \end{aligned}$$

3. FE approximation

The application of the finite element (FE) method to the three-dimensional resistivity problem for isotropic structures was discussed by Pridmore et al. (1981), Zhou and Greenhalgh (2001) and Li and Spitzer (2002). Here, we solve the three-dimensional forward problem for anisotropic structures. According to the variational principal, a true solution of a differential equation gives a stationary value to a functional. For our case of Eq. (8), the functional is total Ohmic dissipative energy in the volume due to the secondary field, it reads

$$\begin{aligned} I(v_\mathrm{s}) &= I(v) - I(v_\mathrm{p}) \\ &= \int_\Omega (\nabla v)^\mathrm{T}\underline{\underline{\rho^{-1}}}\nabla v\,\mathrm{d}\Omega - \int_\Omega (\nabla v_\mathrm{p})^\mathrm{T}\underline{\underline{\rho_p^{-1}}}\nabla v_\mathrm{p}\,\mathrm{d}\Omega \\ &= \int_\Omega [(\nabla v_\mathrm{s})^\mathrm{T}\underline{\underline{\rho^{-1}}}\nabla v_\mathrm{s} + 2(\nabla v_\mathrm{p})^\mathrm{T}\underline{\underline{\rho_s^{-1}}}\nabla v_\mathrm{s}]\,\mathrm{d}\Omega, \end{aligned} \tag{11}$$

where Ω denotes the model volume.

Taking the variation the right-hand side of Eq. (11) with respect to v_s, gives

$$\delta I(v_s) = \int_\Omega 2[(\nabla v_s)^T \underline{\underline{\rho}}^{-1} \nabla \delta v_s + (\nabla v_p)^T \underline{\underline{\rho_s}}^{-1} \nabla \delta v_s] \, d\Omega. \quad (12)$$

After carrying out integration by parts and substituting for the boundary conditions denoted by Eqs. (9) and (10), Eq. (12) becomes

$$\delta I(v_s) = -\delta \int_{\Gamma_\infty} \left[\frac{r \cos(r,n)}{B} v_s^2 + 2r \cos(r,n) \left(\frac{1}{B} - \frac{1}{B_p} \right) v_p v_s \right] d\Gamma. \quad (13)$$

Hence, the solution of the boundary value problem consisting of Eqs. (8)–(10) gives a stationary value to the following functional

$$F(v_s) = \int_\Omega [(\nabla v_s)^T \underline{\underline{\rho}}^{-1} \nabla v_s + 2(\nabla v_p)^T \underline{\underline{\rho_s}}^{-1} \nabla v_s] \, d\Omega + \int_{\Gamma_\infty} \left[\frac{r \cos(r,n)}{B} v_s^2 + 2r \cos(r,n) \times \left(\frac{1}{B} - \frac{1}{B_p} \right) v_p v_s \right] d\Gamma. \quad (14)$$

The model volume Ω is subdivided into rectangular hexahedral elements of constant anisotropic resistivity and the integrals of Eq. (14) thus decompose into a sum of integrals over each element. It reads

$$F(v_s) = \sum_{e=1}^{n_e} \int_{\Omega_e} (\nabla v_s)^T \underline{\underline{\rho}}^{-1} \nabla v_s \, d\Omega + \sum_{\Gamma_\infty} \int_{\Gamma_e} \frac{r \cos(r,n)}{B} v_s^2 \, d\Gamma + 2 \left[\sum_{e=1}^{n_e} \int_{\Omega_e} (\nabla v_p)^T \underline{\underline{\rho_s}}^{-1} \nabla v_s \, d\Omega + \sum_{\Gamma_\infty} \int_{\Gamma_e} r \cos(r,n) \left(\frac{1}{B} - \frac{1}{B_p} \right) v_p v_s \, d\Gamma \right], \quad (15)$$

where Ω_e denotes the volume of a particular element e, Γ_e the surface element on Γ_∞, and n_e the number of elements. The primary and secondary potentials are approximated in each element by linear representations

$$v_p = \sum_{i=1}^{8} N_i v_{p,i}, \qquad v_s = \sum_{i=1}^{8} N_i v_{s,i}, \quad (16)$$

where N_i are linear shape functions (Li and Spitzer, 2002), while $v_{p,i}$ and $v_{s,i}$ are the primary potential and the secondary potential at the corner points i, $i = 1, \ldots, 8$. By Substituting the linear representations (16) into Eq. (15) and evaluating the volume integrals over Ω_e and the boundary integral on Γ_e, we obtain the element integral. Summing up the integrals over all the elements, assembling the element matrices to a system matrix, and setting the first variation of the functional $F(v_s)$ with respect to v_s to zero, results in the finite element equation

$$\mathsf{K} V_s = -\mathsf{P}, \quad (17)$$

where the system matrix K is symmetric and sparsely occupied by non-zero elements, V_s is a vector consisting of the unknown values of the secondary potentials at all nodes, and P is the known vector representing the source distribution due to the anomalous resistivity structure.

This system of linear equations is solved numerically using an incomplete Cholesky preconditioned conjugate gradient method. The Incomplete Cholesky decomposition has been proved to be a fast and efficient preconditioner for three-dimensional resistivity modelling (Zhou and Greenhalgh, 2001; Li and Spitzer, 2002).

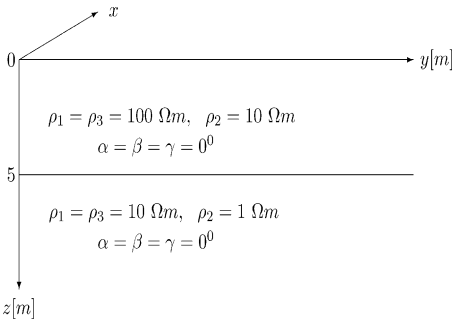

Fig. 1. A two-layer model with azimuthal anisotropy. All three principal axes of the resistivity tensors for both layers are coincident with the (x, y, z) coordinates. The principal resistivities of the first layer and the underlying half-space are $\rho_1/\rho_2/\rho_3 = 100/10/100\ \Omega$ m and $\rho_1/\rho_2/\rho_3 = 10/1/10\ \Omega$ m, respectively.

4. Numerical tests

To test the FE techniques described in the previous sections, a two-layer model with azimuthal anisotropy (Fig. 1) is simulated. Azimuthal means here that only the principal resistivity of one horizontal direction differs from the homogeneous case. All three principal axes of the resistivity tensor for both layers are coincident with the (x, y, z) coordinates, i.e., $\alpha = \beta = \gamma = 0^\circ$. The principal resistivities of the first layer with a thickness of 5 m are assumed to be $\rho_1 = \rho_3 = 100\,\Omega\,\mathrm{m}$, $\rho_2 = 10\,\Omega\,\mathrm{m}$. The principal resistivities of the under-

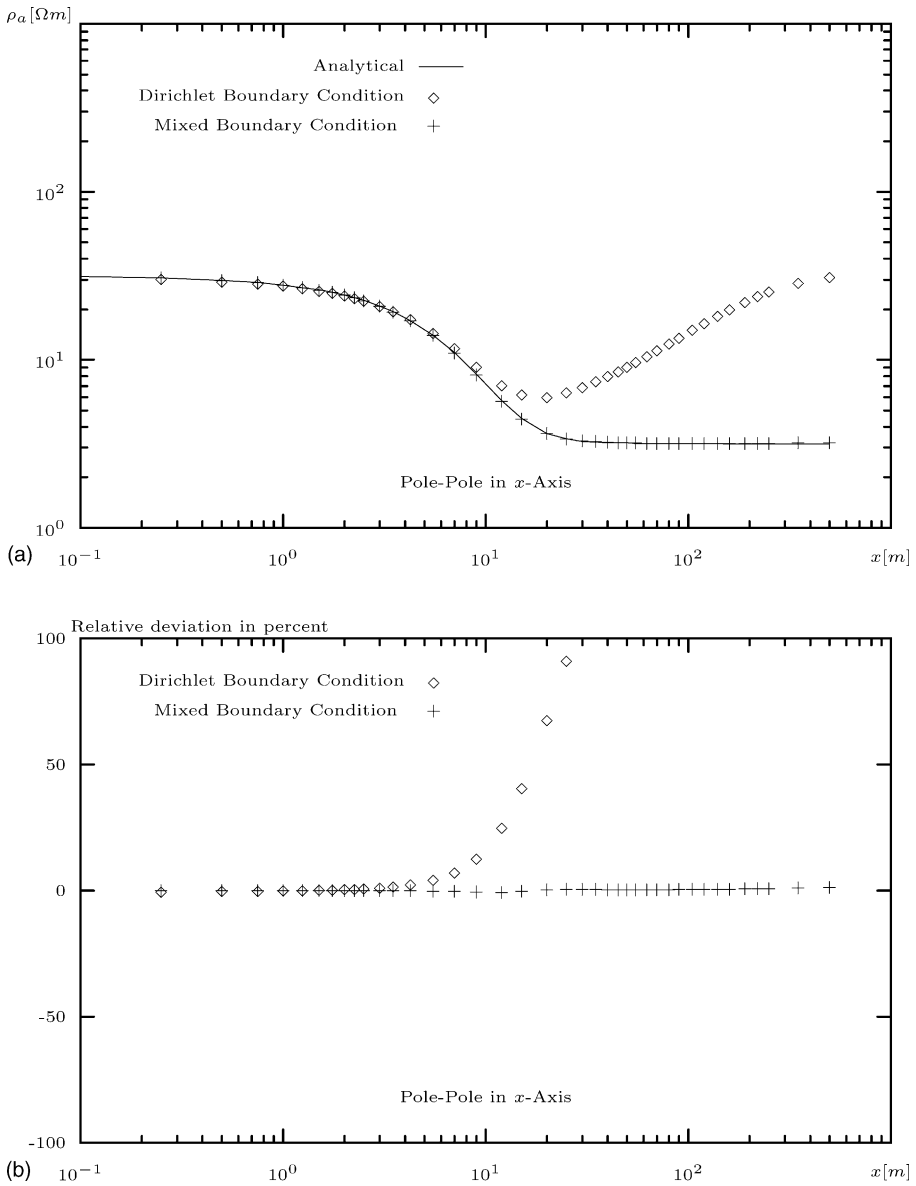

Fig. 2. (a) Apparent resistivity of a pole–pole configuration along the x-axis for the model in Fig. 1. The solid line indicates the analytical solution, diamonds indicate the FE solution for Dirichlet boundary conditions, and crosses indicate the FE solution for mixed boundary conditions. (b) Relative deviation between the FE result and the analytic solution.

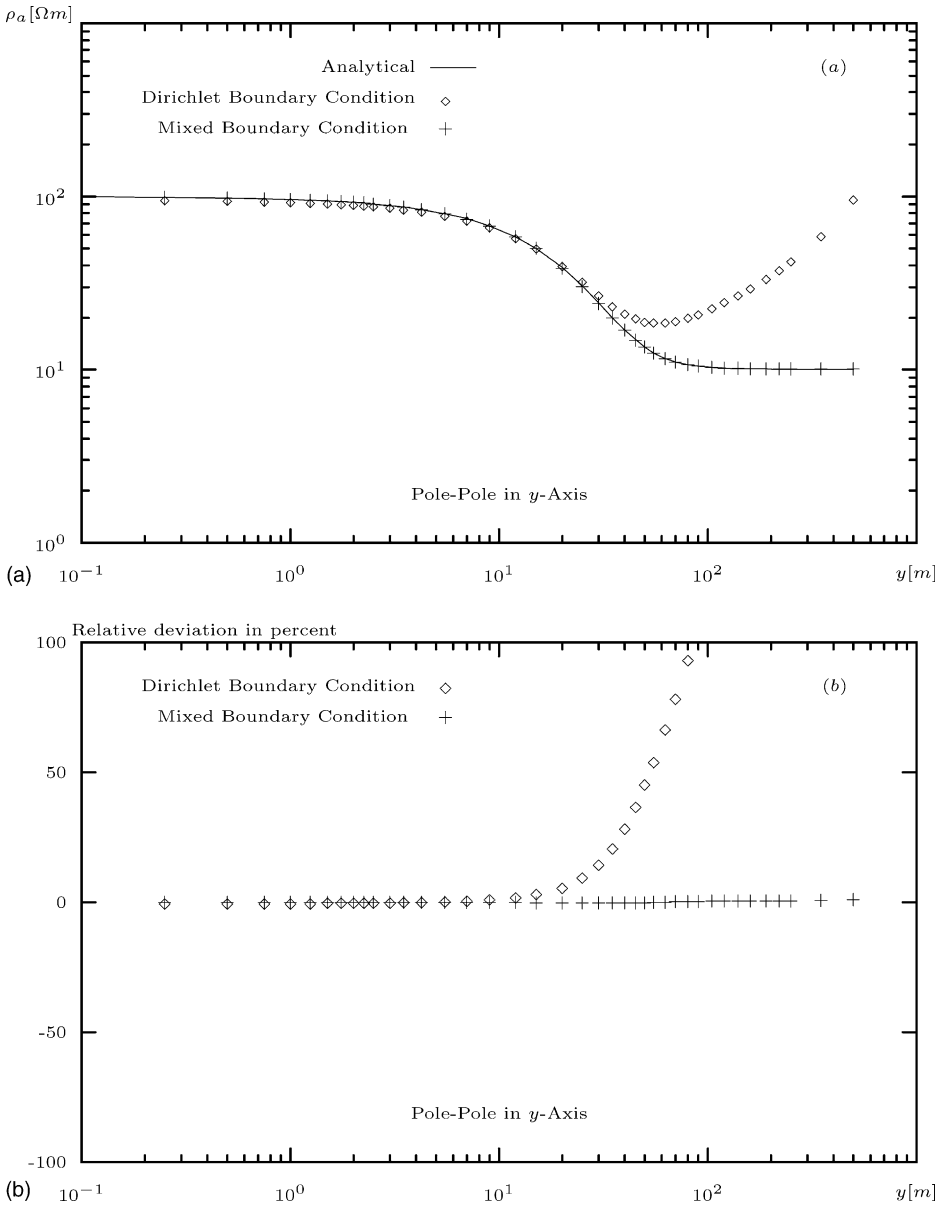

Fig. 3. (a) Apparent resistivity of a pole–pole configuration along the *y*-axis for the model in Fig. 1. (b) Relative deviation between the FE result and the analytic solution. Symbols as in Fig. 2.

lying half-space are assumed to be $\rho_1 = \rho_3 = 10\,\Omega\,\mathrm{m}$, $\rho_2 = 1\,\Omega\,\mathrm{m}$. A pole–pole sounding is carried out along the *x*- and *y*-axis, respectively. The single current source is assumed to be located at the origin of the coordinate system. An irregular grid with $79 \times 79 \times 46$ nodes is used for the FE modelling. The modelling domain boundaries are located at ± 500 m in *x*- and *y*-direction and 500 m in *z*-direction. The homogeneous half-space with azimuthal anisotropy ($\rho_1 = \rho_3 = 100\,\Omega\,\mathrm{m}$, $\rho_2 = 10\,\Omega\,\mathrm{m}$ and $\alpha = \beta = \gamma = 0^\circ$) is regarded as the reference structure for the singularity removal. The FE response is calculated for both Dirichlet and mixed

boundary conditions. In Figs. 2 and 3, apparent resistivity and relative deviation to the analytical solution are plotted versus the electrode distance of a pole–pole configuration in *x*- and *y*-directions, respectively. The analytical solutions according to Wait (1990) are also shown for comparison. The findings are as follows:

(1) The secondary field FE solution for mixed boundary conditions agrees very well with the analytical solution at all grid nodes. Particularly, the algorithm provides accurate results near the source and towards the boundaries. The relative deviation between the numerical results and analytical solution is less than 1.2%.
(2) The FE solution for the homogeneous Dirichlet boundary conditions ($v_s = 0$) agrees well with the analytical result only for small electrode spacings, whereas it shows huge deviations for large electrode spacings. The deviations towards the boundaries are up to about 900%.
(3) For the sounding in *x*-direction, we obtain the expected apparent resistivity of approximately 31.6 Ω m at small electrode spacings, which is the geometric mean of the resistivities of the first layer, and of 3.16 Ω m at large electrode spacings, which is the geometric mean of the resistivities of the underlying half-space.
(4) For the sounding in *y*-direction, we obtain an apparent resistivity of approximately 100 Ω m at small electrode spacings (i.e., the real resistivity of the top layer in *x*-direction) and of 10 Ω m at large electrode spacings (i.e., the real resistivity of the bottom layer in *x*-direction). This is known as the anisotropy paradox.

5. Effects of anisotropy

In this section, a simple anisotropic cube is used to calculate the effect of horizontal, vertical and dipping anisotropy on the geoelectric response. Even though the model is of pronounced simplicity no analytic solution is available. We have chosen such rudimentary model structures to comprehend their physical responses, thereby cross-checking the validity of our code's output.

The cube has a side length of 5 m and is buried at a depth of 0.5 m. It has principal resistivities of $\rho_1/\rho_2/\rho_3 = 100/5/100\,\Omega\,\mathrm{m}$ and is embedded in an isotropic homogeneous half-space with a resistivity of 5 Ω m (Fig. 4). The computed contour maps of the apparent resistivity at the surface are shown for a pole–pole array. The single current source is located at the origin. The whole array rotates around the current electrode. All the calculations are made on a grid of $81 \times 81 \times 47$ nodes.

5.1. Horizontal anisotropy

It is assumed that one principal axis of the resistivity tensor of the cube coincides with the vertical *z*-axis and the remaining two principal axes are in the horizontal plane (x, y) with strike angle α with respect to the *x*-axis. The cube's resistivity tensor has the following form

$$\underline{\underline{\rho}} = \begin{pmatrix} \rho_1 \cos^2\alpha + \rho_2 \sin^2\alpha & (\rho_1 - \rho_2)\sin\alpha\cos\alpha & 0 \\ (\rho_1 - \rho_2)\sin\alpha\cos\alpha & \rho_1 \sin^2\alpha + \rho_2 \cos^2\alpha & 0 \\ 0 & 0 & \rho_3 \end{pmatrix}.$$

Fig. 5 shows the contour maps of the apparent resistivity for three different angles $\alpha = 0^\circ, 45^\circ, 90^\circ$. For small distances between current source and measuring point, the influence of the anisotropic cube can hardly be seen. With increasing distance the influence becomes more and more obvious as the contours become stretched. The maximum and minimum axes indicate the direction of the low and high resistivity, respectively, which is again due to the anisotropy paradox. Far from the inhomogeneity, the anomalous field fades out and ρ_a approaches the resistivity of the isotropic half-space. Note the agreement of the results for $\alpha = 0^\circ$ and 90° except for the rotation of 90°. This is a very basic test on a correctly coded numerical program especially with respect to the incorporation of the boundary conditions on the outside domain boundaries.

5.2. Dipping anisotropy

It is assumed that one principal axis of resistivity tensor of the cube coincides with the horizontal *x*-axis and the remaining two principal axes are in the vertical plane (y, z) with strike angle β with respect to the *y*-axis.

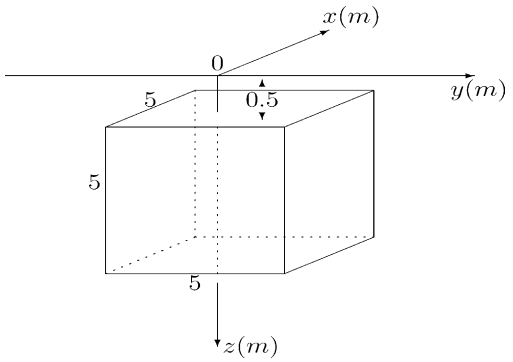

Fig. 4. A three-dimensional anisotropic cube with a side length of 5 m buried at a depth of 0.5 m, embedded in a homogeneous isotropic half-space of resistivity 5 Ω m. The principal resistivities of the cube are given by $\rho_1/\rho_2/\rho_3 = 100/5/100\,\Omega\,\mathrm{m}$.

The cube's resistivity tensor has the following form

$$\underline{\underline{\rho}} = \begin{pmatrix} \rho_1 & 0 & 0 \\ 0 & \rho_2\cos^2\beta + \rho_3\sin^2\beta & (\rho_2-\rho_3)\sin\beta\cos\beta \\ 0 & (\rho_2-\rho_3)\sin\beta\cos\beta & \rho_2\sin^2\beta + \rho_3\cos^2\beta \end{pmatrix}.$$

Fig. 6 shows the contour maps of the apparent resistivity for three dip angles $\beta = 30^\circ, 45^\circ, 60^\circ$. Again, for small distances the influence of the anisotropic cube can hardly be seen. For larger distances the contours are non-symmetric with respect to the x-axis ($y = 0$) and are elongated in the x- and y-directions at the right-hand side of the map. Note the existence of two resistivity maxima left and right to the source point. Their magnitudes change with the dip angle β. It can more clearly be understood in the apparent resistivity curves along the y-axis shown in Fig. 7. We may explain this behavior by the distribution of the current density in the earth. In an anisotropic medium, the current density is generally given by a linear combination of all three components of the electric field. From Eqs. (1) and (3), and $\sigma_{yx} = \sigma_{zx} = 0$, the y- and z-components of the current density in the yz-plane are expressed by

$$j_y(0, y, z) = -\sigma_{yy}\frac{\partial v}{\partial y} - \sigma_{yz}\frac{\partial v}{\partial z}, \tag{18}$$

$$j_z(0, y, z) = -\sigma_{yz}\frac{\partial v}{\partial y} - \sigma_{zz}\frac{\partial v}{\partial z}. \tag{19}$$

Fig. 8 shows the distribution of the current density in the yz-plane for three dipping angles $\beta = 30^\circ, 45^\circ, 60^\circ$. Since the current density decays very quickly with the distance to the current source, it is scaled at each point by r^2 according to Yin and Maurer (2001), thereby obtaining a better visualization (r is the source–receiver separation). This scaling is equivalent to the normalization by the far-field. From Fig. 8, one can clearly see that magnitude and direction of the current density change with the dipping angle β, and the current flows mainly in the direction of the low resistivity.

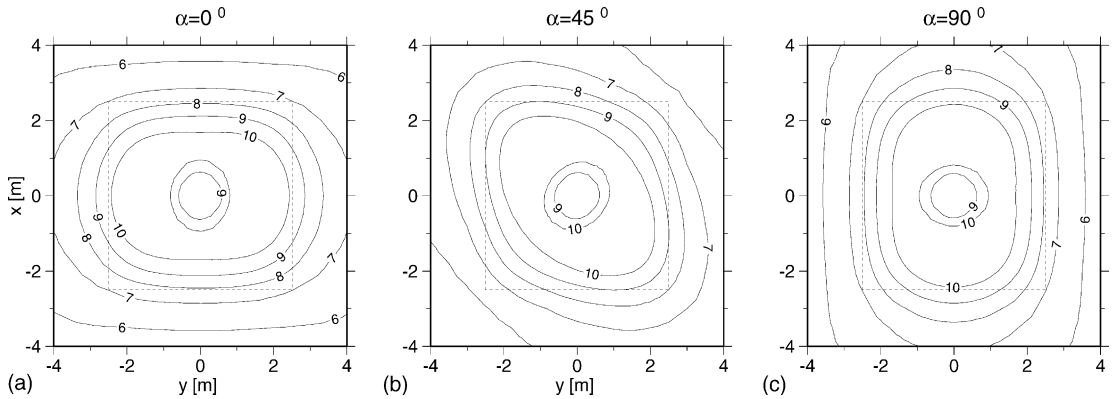

Fig. 5. Contour maps of the apparent resistivity for a pole–pole configuration over a three-dimensional cube model with horizontal anisotropy buried in an isotropic half-space with $\rho = 5\,\Omega\,\mathrm{m}$: (a) for strike angle $\alpha = 0^\circ$; (b) for $\alpha = 45^\circ$; (c) for $\alpha = 90^\circ$. The cube has a side length of 5 m and its resistivity tensor is given by the principal resistivities of $\rho_1/\rho_2/\rho_3 = 100/5/100\,\Omega\,\mathrm{m}$ for varying anisotropic strike angles α. The dotted lines indicate the cube's outline.

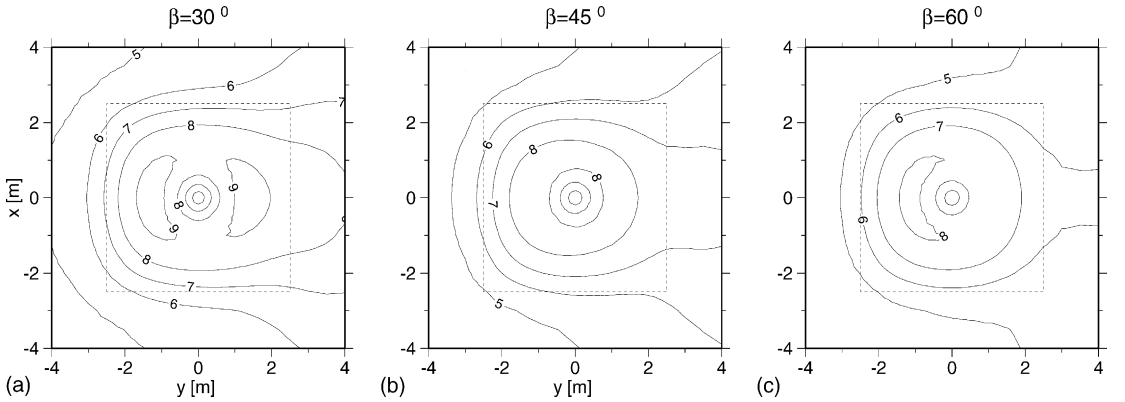

Fig. 6. Contour maps of the apparent resistivity for a pole–pole configuration over a three-dimensional cube model with dipping anisotropy: (a) for dipping angle $\beta = 30^\circ$; (b) for $\beta = 45^\circ$; (c) for $\beta = 60^\circ$. The cube's resistivity tensor is given by the principal resistivities of $\rho_1/\rho_2/\rho_3 = 100/5/100\,\Omega\,\mathrm{m}$ for varying dipping angles β. The dotted lines indicate the cube's outline.

5.3. Vertical anisotropy

It is assumed that all three principal axes of the cube's resistivity tensor are coincident with the axes of (x, y, z) coordinates and the resistivity is axially symmetric with respect to z, i.e., the resistivity for any horizontal direction differs solely from that in vertical direction. Fig. 9 shows the contour map of the apparent resistivity, which is identical with the dipping anisotropy for $\beta = 90^\circ$. The contours are nearly circles centered at the origin. Again this represents a plausible response. Furthermore, this implies that the vertical anisotropy cannot be seen from geoelectrical surface data.

6. Tensor apparent resistivity

The classical dc resistivity techniques (e.g., Schlumberger, Wenner, dipole–dipole, etc.) measure only a single component of the electric field, where the direction of the electric field is completely ignored. When two current bipolar sources with different orientations are used and both components of the electric field are measured for each current bipole, the apparent resistivity tensor and its three rotational invariants P_1, P_2 and P_3 can be defined (Bibby, 1986). These tensor invariants have considerable advantages over the scalar apparent resistivities and are virtually unperturbed beyond the

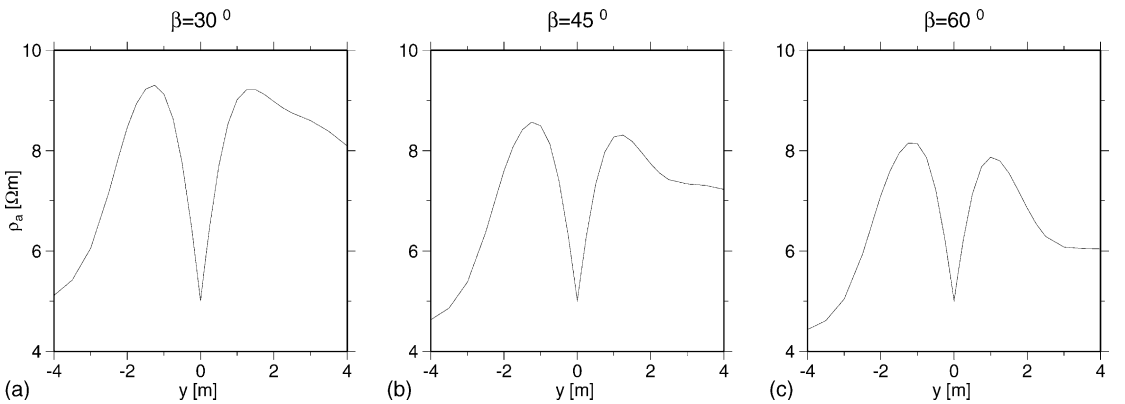

Fig. 7. Sounding curves along the y-axis for a pole–pole configuration over the three-dimensional cube model from Fig. 5 with dipping anisotropy: (a) for dipping angle $\beta = 30^\circ$; (b) for $\beta = 45^\circ$; (c) for $\beta = 60^\circ$.

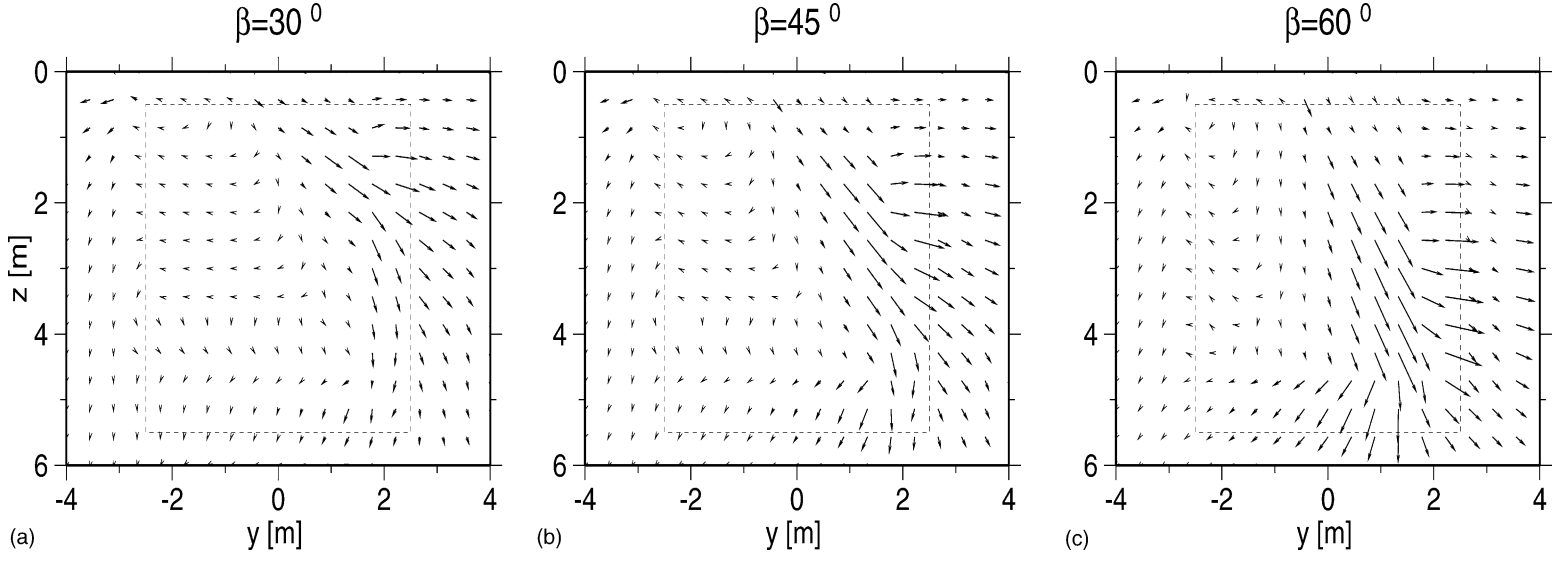

Fig. 8. The distribution of the current density in the yz-plane for the cube model of Fig. 5 with dipping anisotropy: (a) for dipping angle $\beta = 30^\circ$; (b) for $\beta = 45^\circ$; (c) for $\beta = 60^\circ$. The dotted lines indicate the cube's outline.

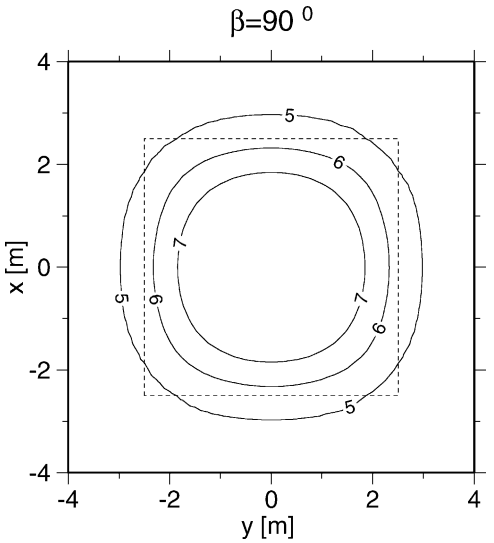

Fig. 9. A contour map of the apparent resistivity for the pole–pole configuration over a three-dimensional cube with vertical anisotropy. The dotted lines indicate the cube's outline.

extent of the inhomogeneity. According to Bibby and Hohmann (1993) the invariant P_2 gives the best representation of a three-dimensional buried inhomogeneity. In this section, we will present some P_2 invariants for anisotropic structures and show that this does not hold when anisotropy is present.

Again, we consider the anisotropic cube model from the previous section, however, buried in an isotropic half-space of 100 Ω m. Two bipolar sources are located at (−157 m, 450 m) and (163 m, 130 m), and (−157 m, 130 m) and (163 m, 450 m) (Fig. 10). These locations are chosen off from given main grid geometries in order to recognize possible artifacts that are due to grid symmetries. It furthermore shows that the code allows for arbitrary source configurations. Fig. 11 shows the P_2 invariant for horizontal anisotropy with $\alpha = 45^\circ, \beta = \gamma = 0^\circ$ (Fig. 11a), and dipping anisotropy with $\beta = 60^\circ, \alpha = \gamma = 0^\circ$ (Fig. 11b), and for general anisotropy with $\alpha = 45^\circ, \beta = 60^\circ, \gamma = 0^\circ$ (Fig. 11c). For comparison, P_2 is also shown for an isotropic cube having a resistivity that equals the geometric mean of the cube's main resistivity of 22.36 Ω m (Fig. 11d). From these figures, one can see that P_2 is very sensitive to anisotropy and it does not reflect the shape of the three-dimensional inhomogeneity anymore.

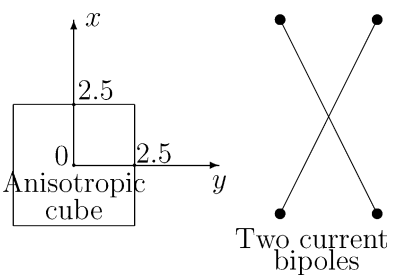

Fig. 10. Schematic diagram of configuration of two current bipoles.

7. Discussion and conclusions

In this paper, we have presented a newly developed finite element algorithm for numerical modelling of geoelectrical fields in arbitrarily anisotropic three-dimensional structures. We have not intended to discuss the effects of anisotropy in general. This has been done in a number of papers in the past. We have taken an analytical solution to check our newly developed code for accuracy in a special case. Due to the lack of further closed analytical solutions to the anisotropic equation of continuity, we extrapolate the accuracy of the results to more complex model geometries knowing that this is just an assumption. However, this is the legitimate way of cross-checking numerical software. If there were enough other solutions, indeed, our code would not be necessary.

We do not discuss known drawbacks of the secondary potential solution either, since any code employing this formulation encounters the same troubles when, e.g., the resistivity at the electrodes differs from the reference resistivity or when two source electrodes are placed within different conductivity environments. This is not specific for an anisotropy code and therefore neglected in this paper.

Choosing a variety of representative but still simple three-dimensional models, we have shown that our code works well to the best of our knowledge and belief and that it is ready to be used by practitioners in the scientific community. Tests have shown that our method consumes about the same computation time as it would take to model isotropic structures, so run times are within the expected range for regular three-dimensional dc codes.

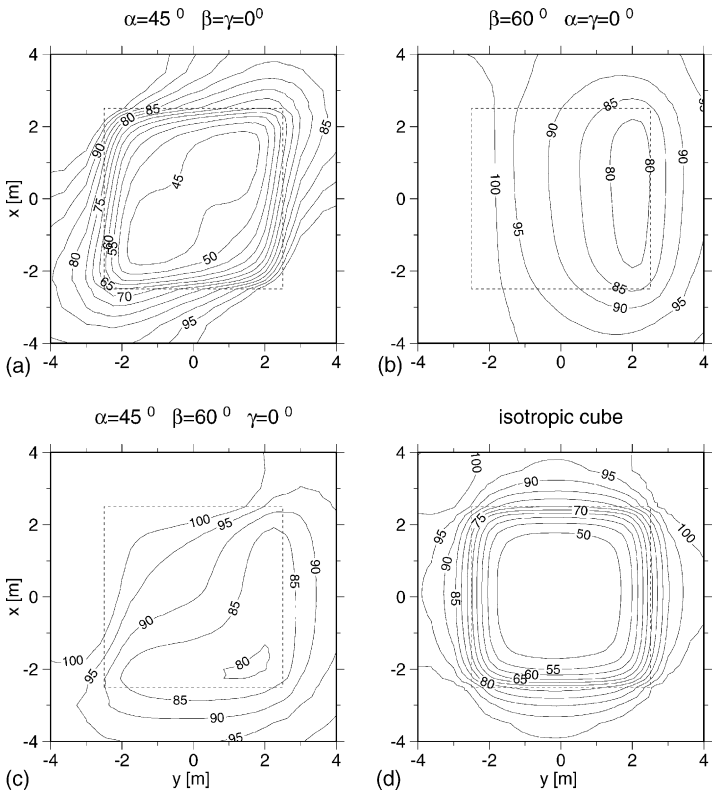

Fig. 11. The P_2 invariant over a three-dimensional cube model with horizontal anisotropy (a), with dipping anisotropy (b), with general anisotropy (c) and for an isotropic cube (d). The dotted lines indicate the cube's outline. Note that P_2 for anisotropic cubes does not reflect the shape of the three-dimensional inhomogeneity anymore.

Acknowledgments

This work was supported by the Deutsche Forschungsgemeinschaft (Ja 590/18-1). We would like to thank Yasuo Ogawa and an anonymous reviewer for critical reviews and comments.

Appendix A. Mixed boundary condition for a generally anisotropic medium

The electrical potential due to a point source on the surface of a homogeneous, generally anisotropic half-space can be constructed by successively applying three rotations to the coordinate system underlying Eq. (7). A point source located at $(x_q, y_q, 0)$ then yields

$$v_p = \frac{I}{2\pi}\frac{(\rho_1^p\rho_2^p\rho_3^p)^{1/2}}{B_p^{1/2}}, \tag{A.1}$$

with

$$B_p = \rho_{xx}^p(x-x_q)^2 + 2\rho_{xy}^p(x-x_q)(y-y_q) + 2\rho_{xz}^p(x-x_q)z + \rho_{yy}^p(y-y_q)^2 + 2\rho_{yz}^p(y-y_q)z + \rho_{zz}^p z^2.$$

Here, ρ_1^p, ρ_2^p, and ρ_3^p are the principal resistivities , ρ_{xx}^p, ρ_{xy}^p, …, ρ_{zz}^p are six components of resistivity tensor of the homogeneous anisotropic half-space. From Eq. (A.1), we can get

$$\underline{\underline{\rho_p^{-1}}}\frac{\partial v_p}{\partial n} = \underline{\underline{\sigma_p}}\nabla v\cdot\boldsymbol{n} = -\frac{I(\rho_1^p\rho_2^p\rho_3^p)^{1/2}}{2\pi B_p^{3/2}} \times \begin{pmatrix}\sigma_{xx}^p & \sigma_{xy}^p & \sigma_{xz}^p\\ \sigma_{xy}^p & \sigma_{yy}^p & \sigma_{yz}^p\\ \sigma_{xz}^p & \sigma_{yz}^p & \sigma_{zz}^p\end{pmatrix}\begin{pmatrix}\rho_{xx}^p(x-x_q)+\rho_{xy}^p(y-y_q)+\rho_{xz}^p z\\ \rho_{xy}^p(x-x_q)+\rho_{yy}^p(y-y_q)+\rho_{yz}^p z\\ \rho_{xz}^p(x-x_q)+\rho_{yz}^p(y-y_q)+\rho_{zz}^p z\end{pmatrix}\cdot\boldsymbol{n},$$

where $\boldsymbol{n}$ is the outward normal direction. After some algebraic calculations, we have

$$\underline{\underline{\rho_p^{-1}}}\frac{\partial v_\mathrm{p}}{\partial n} = -\frac{I(\rho_1^\mathrm{p}\rho_2^\mathrm{p}\rho_3^\mathrm{p})^{1/2}}{2\pi {B_\mathrm{p}}^{3/2}}\boldsymbol{r}\cdot\boldsymbol{n} = -\frac{r\cos(r,n)}{B_\mathrm{p}}v_\mathrm{p},$$

or

$$\underline{\underline{\rho_p^{-1}}}\frac{\partial v_\mathrm{p}}{\partial n} + \frac{r\cos(r,n)}{B_\mathrm{p}}v_\mathrm{p} = 0, \tag{A.2}$$

where $r = ((x-x_\mathrm{q})^2 + (y-y_\mathrm{q})^2 + z^2)^{1/2}$ denotes the radial distance from the source location to a measuring point.

If the outer domain boundary is far enough away from the source as well as from the inhomogeneity, the anomalous potential caused by the inhomogeneity is assumed to be zero. Then, the total potential on Γ_∞ can be approximated by

$$v = \frac{I}{2\pi}\frac{(\rho_1\rho_2\rho_3)^{1/2}}{B^{1/2}} \quad \text{on } \Gamma_\infty, \tag{A.3}$$

with

$$\begin{aligned} B = {} & \rho_{xx}(x-x_\mathrm{q})^2 + 2\rho_{xy}(x-x_\mathrm{q})(y-y_\mathrm{q}) \\ & + 2\rho_{xz}(x-x_\mathrm{q})z + \rho_{yy}(y-y_\mathrm{q})^2 \\ & + 2\rho_{yz}(y-y_\mathrm{q})z + \rho_{zz}z^2. \end{aligned}$$

From Eq. (A.3), we can get the following relation

$$\underline{\underline{\rho^{-1}}}\frac{\partial v}{\partial n} + \frac{r\cos(r,n)}{B}v = 0 \quad \text{on } \Gamma_\infty. \tag{A.4}$$

Substituting Eq. (5) into (A.4) and using Eq. (A.2), we get the relation in Eq. (10).

References

Bibby, H.M., 1978. Direct current resistivity modeling for axially symmetric bodies using finite element method. Geophysics 43, 550–562.

Bibby, H.M., 1986. Analysis of multiple-source bipole–quadrupole resistivity surveys using the apparent resistivity tensor. Geophysics 51, 872–983.

Bibby, H.M., Hohmann G.W., 1986. Three-dimensional interpretation of multiple-source bipole–dipole resistivity data using the apparent resistivity tensor. Geophys. Prospecting 41, 693–723.

Bhattacharya, P.K., Patra, H.P., 1968. Direct current geoelectric sounding. Methods in Geochemical and Geophysical Series 9. Elsevier, Amsterdam.

Busby, 2000. The effectiveness of azimuthal apparent resistivity measurements as a method for determining fracture strike orientations. Geophys. Prospecting 48, 677–695.

Coggon, J.H., 1971. Electromagnetic and electrical modelling by the finite element method. Geophysics 36, 132–155.

Dey, A., Morrison, H.F., 1979. Resistivity modelling for arbitrarily shaped three-dimensional structures. Geophysics 44, 615–632.

Habberjam, G.M., 1979. Apparent resistivity observations and the use of square array techniques. Geoexploration Monograph Series 9. Gebrüder Borntraeger, Berlin.

Leonard-Mayer, P.J., 1984. A surface resistivity method for measuring hydrologic characteristics of jointed formations. Report of Investigations 8901, Bureau of Mines, United States Department of the Interior.

Li, P., Uren, N.F., 1997. Analytical solution for the point source potential in an anisotropic 3-D half-space. I. Two-horizontal-layer case. Math. Comput. Model. 26, 9–27.

Li, Y., Spitzer, K., 2002. Three-dimensional dc resistivity forward modelling using finite elements in comparison with finite-difference solutions. Geophys. J. Int. 151, 924–934.

Lowry, T., Allen, M.B., Shive, P.N., 1989. Singularity removal: a refinement of resistivity modeling techniques. Geophysics 54, 766–774.

Pridmore, D., Hohmann, G.W., Ward, S.H., Sill, W.R., 1981. An investigation of finite element modeling for electrical and electromagnetic modeling data in three dimensions. Geophysics 46, 1009–1024.

Taylor, R.W., Fleming, A.H., 1988. Characterizing jointed systems by azimuthal resistivity surveys. Ground water 26, 464–474.

Verner, T., Pek, J., 1998. Numerical modelling of direct currents in 2-D anisotropic structures. In: Bahr, K., Junge, A. (Eds.), Elektromagnetische Tiefenforschung. Deutsche Geophysikalische Gesellschaft, pp. 228–237.

Wait, J.R., 1990. Current flow into a 3-dimensionally anisotropic conductor. Radioscience 25, 689–694.

Watson, K.A., Barker, R.D., 1999. Differentiating anisotropy and lateral effects using azimuthal resistivitiy offset Wenner soundings. Geophysics 64, 739–745.

Yin, Ch., Weidelt, P., 1999. Geoelectrical fields in a layered earth with arbitrary anisotropy. Geophysics 64, 426–434.

Yin, Ch., Maurer, H.M., 2001. Electromagnetic induction in a layered earth with arbitrary anisotropy. Geophysics 66, 1405–1416.

Zhao, S., Yedlin, M., 1996. Some refinements on the finite-difference method for 3-D dc resistivity modelling. Geophysics 61, 1301–1307.

Zhou, B., Greenhalgh, S.A., 2001. Finite element three-dimensional direct current resistivity modeling: accuracy and efficiency considerations. Geophys. J. Int. 145, 679–688.